VIP Thermoelectric Materials Very Important Paper

Deutsche Ausgabe: DOI: 10.1002/ange.201713223
Internationale Ausgabe: DOI: 10.1002/anie.201713223

Manipulating Band Structure through Reconstruction of Binary Metal Sulfide for High-Performance Thermoelectrics in Solution-Synthesized Nanostructured $Bi_{13}S_{18}I_2$

*Biao Xu[+], Tianli Feng[+], Matthias T. Agne, Qing Tan, Zhe Li, Kazuki Imasato, Lin Zhou, Je-Hyeong Bahk, Xiulin Ruan, G. Jeffery Snyder, and Yue Wu**

Abstract: *Reconstructing canonical binary compounds by inserting a third agent can significantly modify their electronic and phonon structures. Therefore, it has inspired the semiconductor communities in various fields. Introducing this paradigm will potentially revolutionize thermoelectrics as well. Using a solution synthesis, Bi_2S_3 was rebuilt by adding disordered Bi and weakly bonded I. These new structural motifs and the altered crystal symmetry induce prominent changes in electrical and thermal transport, resulting in a great enhancement of the figure of merit. The as-obtained nanostructured $Bi_{13}S_{18}I_2$ is the first non-toxic, cost-efficient, and solution-processable n-type material with $zT = 1.0$.*

Thermoelectrics, in which the waste heat can be converted into electricity in a silent and reliable way, have gained renewed interests.[1] The semiconductor industry, of which thermoelectrics is a subset, has been primarily relying on binary compounds. Specifically, the state-of-the-art thermoelectric compounds are Bi_2Te_3[2] operating at low-temperature (300–500 K) and PbTe,[3] SnSe,[4] and $CoSb_3$[5] at medium temperature (500–900 K). The conversion efficiency of thermoelectrics is evaluated by the figure of merit, $zT = S^2\sigma T/\kappa$. Typical ways to enhance the zT of these binary compounds include increasing the power factor, $S^2\sigma$, through band engineering, such as energy filtering,[6] resonant level,[7] and/or diminishing κ via structural engineering, as exemplified by the atomic-level defect[8] nanoscale grain boundary.[9]

Aside from performance, cost and toxicity also raise critical concerns. Since Co and Pb are toxic and Te is also scarce (0.001 ppm in earth crust), the earth-abundant (500 ppm) and eco-friendly sulfur-based counterparts have attracted attentions as potential alternatives.[10] However, their performance is impaired by lower carrier mobility (μ) owing to the more ionic bonding and higher κ ascribed to the lower atomic weight. The commonly used strategies to improve zT have encountered a bottleneck to achieve $zT = 1.0$ in binary metal sulfides, especially for the n-type leg.

Recently, dismantling and reconstructing the canonical binary compound by inserting a third agent[11] has inspired material explorations in various fields, such as electronic devices (SnS_2-$(N_2H_5)_4Sn_2S_6$)[12] and radiation detectors (HgS-$Cs_2Hg_6S_7$).[13] This strategy may also reconstruct the crystal structure of binary thermoelectric compounds, resulting in possible modifications of electronic and phonon structures. However, it has seldom been attempted, which is probably due to the synthetic complexity and the sophisticated interplay between the transport properties[1] (S, σ, and κ). Herein, we chose the n-type binary metal sulfide, Bi_2S_3 and inserted a third environmentally compatible and earth-abundant element, iodine. The resultant $Bi_{13}S_{18}I_2$ has the crystal symmetry changed and several novel structural motifs introduced, leading to substantially modified electronic and phonon structures. Consequently, it significantly outperformed the parent compound (Bi_2S_3). The high zT (1.0 at 788 K), as well as eco-friendly and cost-efficient constituent elements qualify this material as a competitive alternative to conventional Te-based thermoelectrics.

$Bi_{13}S_{18}I_2$ has a complex crystal structure that belongs to a trigonal lattice with the space group $P3$.[14] There are four sites for disordered Bi(X), each with a $^1/_4$ occupancy. These disordered Bi(X) atoms at the (1/3, 2/3, z) sites coordinate with six S atoms to form a wheel-like cluster (Figure 1a). The Bi(X) atom disorder and Bi–Bi bonding had been validated through both single-crystal and powder X-ray diffraction in previous studies.[14] This unusual Bi–Bi bond had also been witnessed in $CsBi_4Te_6$[15] and BiTe.[16] Between the disordered Bi(X) atoms, the Bi_4S_6 clusters serve as the connecting arms

[*] Prof. Dr. B. Xu,[+] Z. Li, Prof. Dr. Y. Wu
Department of Chemical and Biological Engineering
Iowa State University, Ames, IA 50011 (USA)
E-mail: yuewu@iastate.edu
Prof. Dr. B. Xu[+]
College of Chemical Engineering
Nanjing University of Science and Technology
Nanjing, Jiangsu 210094 (China)
Dr. T. Feng,[+] Prof. Dr. X. Ruan
Department of Mechanical Engineering, Purdue University
West Lafayette, IN 47907 (USA)
M. T. Agne, K. Imasato, Prof. Dr. G. J. Snyder
Department of Materials Science and Engineering
Northwestern University, Evanston, IL 60208 (USA)
Dr. Q. Tan
State Key Laboratory for Advanced Metals and Materials
University of Science and Technology Beijing
Beijing 100083 (China)
Prof. Dr. L. Zhou
Ames Laboratory, Department of Energy, Ames, IA 50011 (USA)
Prof. Dr. J. H. Bahk
Department of Mechanical and Materials Engineering
University of Cincinnati, Cincinnati, OH 45221 (USA)
[+] These authors contributed equally to this work.
Supporting information and the ORCID identification number(s) for the author(s) of this article can be found under: https://doi.org/10.1002/anie.201713223.

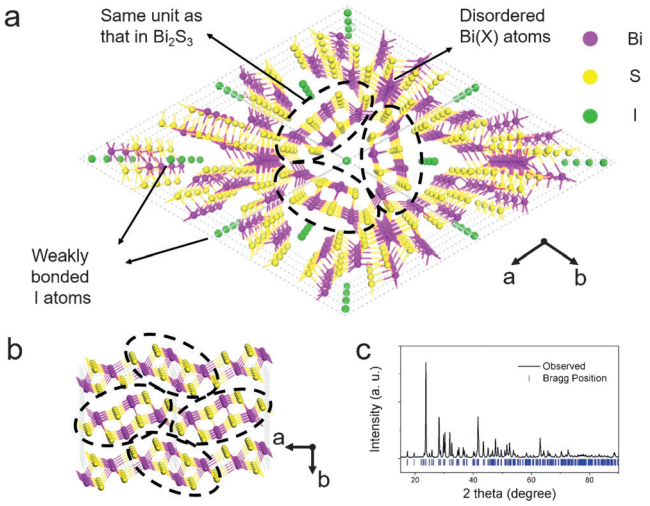

Figure 1. The crystal structure of a) $Bi_{13}S_{18}I_2$ vs. b) Bi_2S_3. The dashed circles illustrate the inherited fragment in $Bi_{13}S_{18}I_2$ from Bi_2S_3. c) The powder X-ray diffraction (PXRD) profile of the bulk $Bi_{13}S_{18}I_2$.

(Figure 1 a). The Bi–S coordination styles in these clusters (Figure 1 a, circled region) are almost the same with those in Bi_2S_3 (Figure 1 b, circled region). These Bi and S atoms construct a 3D framework and create two one-dimensional tunnels propagating along the [001] axis in each unit cell, inside which the I atoms reside. It is noteworthy that the distance between iodine and the nearest atom (Bi) is around 3.57 Å, which is much longer than the sum (2.79 Å) of the covalent radii of Bi (1.46 Å) and I (1.33 Å). This is reminiscent of open framework compounds as exemplified by clathrate ($Ba_8Ga_{16}Ge_{30}$)[17] or $CoSb_3$-based skutterudite.[5] The addition of disordered Bi sites, Bi–Bi bonds, and the iodine sublattice going from Bi_2S_3 to $Bi_{13}S_{18}I_2$ are likely to alter its electronic and thermal properties.

Bulk polycrystalline samples of $Bi_{13}S_{18}I_2$ (6.70 g cm^{-3}, relative density: 96.4 %) could be prepared from spark plasma sintering (SPS) commercial Bi_2S_3 and BiI_3 (the molar ratio is 5.60:1) at 600 °C. We have conducted an analysis of the powder X-ray diffraction (PXRD) profile of the bulk $Bi_{13}S_{18}I_2$ and confirmed this single-phase product (Figure 1 c). The Rietveld refinement was also carried out (Supporting Information, Table S1 and Figure S2). Energy dispersive spectrum (EDS) detected the chemical composition (measured at. %: Bi 40.1, S 53.6, I 6.3, theoretical at. % of $Bi_{13}S_{18}I_2$: Bi 39.3, S 54.5, I 6.1).

Along with the bulk $Bi_{13}S_{18}I_2$ prepared, we have also adopted a solution-phase method to synthesize the nanocrystalline counterpart, which was then unequivocally characterized by various techniques. First, the PXRD pattern agreed well with the simulated one (Supporting Information, Figure S6). Furthermore, EDS confirmed the chemical composition (at. %: Bi 39.0, S 55.0, I 6.0, theoretical at. %: Bi 39.3, S 54.5, I 6.1). Finally, transmission electron microscopy (TEM) depicted the microstructure of the product. As expected from the trigonal crystal structure of $Bi_{13}S_{18}I_2$, an anisotropic rod-like shape could be found (Figure 2 a). The axial direction of the nanorod was indexed as [001] by high-

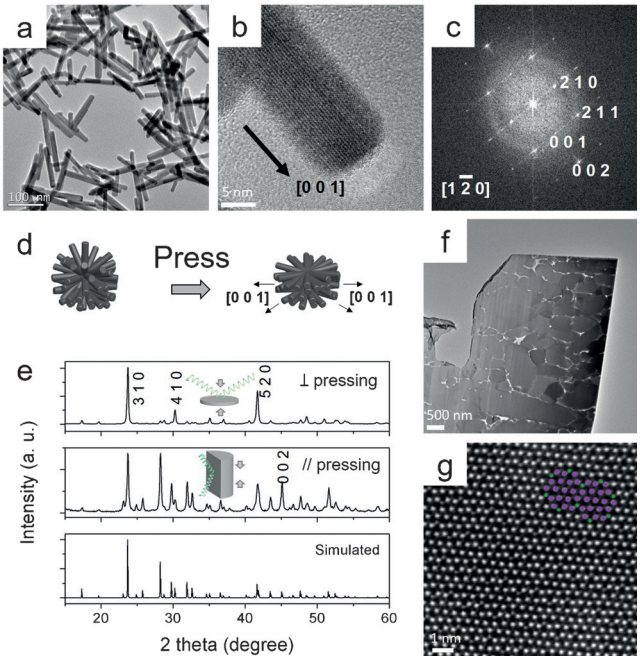

Figure 2. a) Low-magnification and b) high-resolution TEM images of $Bi_{13}S_{18}I_2$ nanorods, c) fast Fourier transform pattern, d) illustration of the spark plasma sintering process that induced the crystallographic anisotropy, e) PXRD patterns of the as-sintered nanostructured material along different directions and the simulated pattern, f) TEM image of a focused-ion-beam-cut thin section of the as-sintered nano $Bi_{13}S_{18}I_2$, g) HAADF-STEM image of an as-sintered nano $Bi_{13}S_{18}I_2$, showing the hexagonal periodicity of I atoms as darker dots (green spheres) and Bi atoms as brighter dots (purple spheres).

resolution transmission electron microscopy (HRTEM, Figure 2 b,c).

The scalable (9.0 g per batch) synthesis of $Bi_{13}S_{18}I_2$ nanopowder enabled us to consolidate it into a macroscopic cylinder (diameter 10 mm × height 12 mm, 6.33 g cm^{-3} relative density = 91.1 %). After SPS, the crystal phase was preserved according to PXRD (Figure 2 e). From the TEM (Figure 2 f) of the focused-ion-beam (FIB)-cut nanosample, the grain size was estimated to be 800 ± 300 nm. EDS corroborated the nearly identical atomic percentages of Bi, S, and I (at. %: Bi 39.4, S 54.3, I 6.3) to nominal values (at. %: Bi 39.3, S 54.5, I 6.1). HRTEM clearly revealed the lattice fringe of (100), (001) plane and honeycomb-like pattern along [001] axis (Supporting Information, Figure S7). The atomically resolved high-angle annular dark-field scanning transmission electron microscopy (HAADF-STEM) image taken along [001] zone axis was in good accordance with the atomic model (Figure 2 g). $BiCl_3$ was mixed with the $Bi_{13}S_{18}I_2$ nanopowder (Supporting Information, Figure S8c–f) and then SPSed to study the dopant effect.

Interestingly, the as-compressed nanostructured material manifested a strong crystallographic anisotropy (Figure 2 e). In the cross-plane (⊥ pressing) XRD, (hk0) reflection peaks, such as (310), (410) and (520), were notably enhanced. In stark contrast, in the in-plane (∥ pressing) XRD, (002) peak was relatively much stronger. This anisotropy might stem from the anisotropic grain structure of the starting crystallite

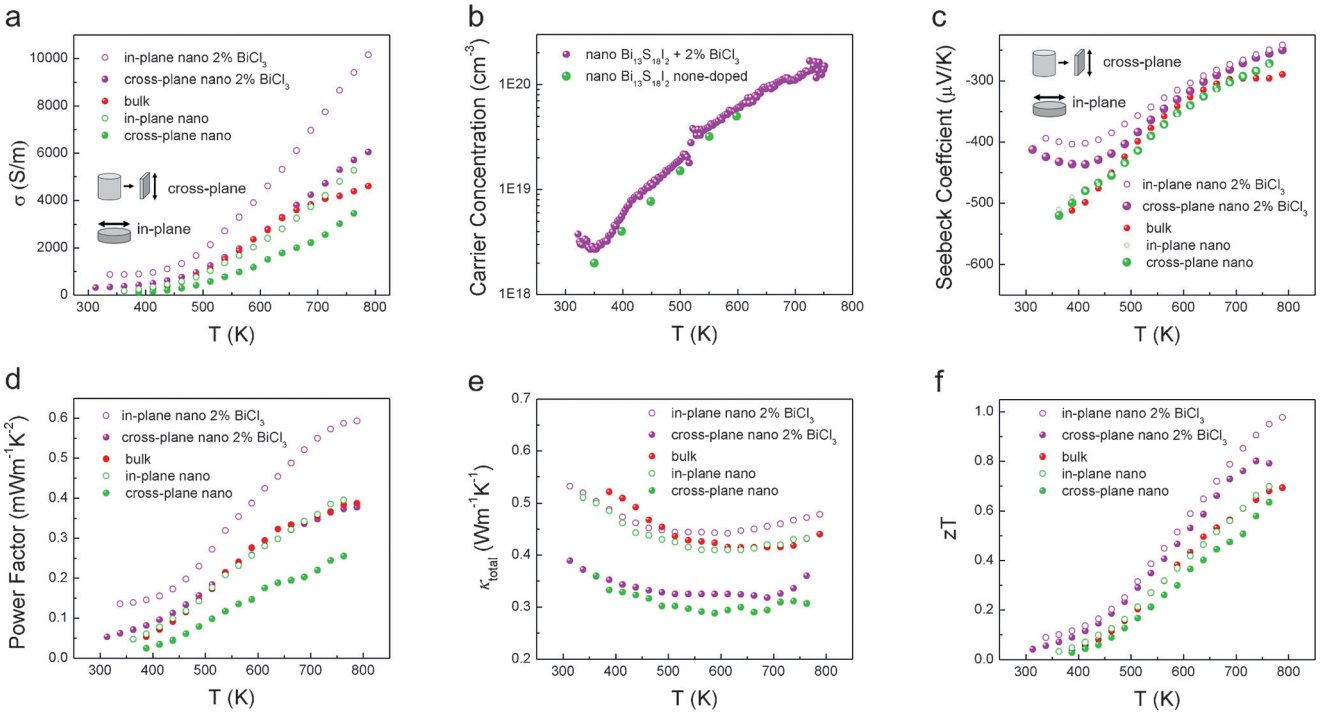

Figure 3. Temperature dependence of a) electrical conductivity, b) Hall carrier concentration, c) Seebeck coefficient, d) power factor, e) total thermal conductivity, f) Figure of merit, zT, of the three $Bi_{13}S_{18}I_2$ samples: "bulk", "nano" (no $BiCl_3$ added), and "nano with 2% $BiCl_3$".

of nanorods as the long axis ([001] direction) of the nanorod tended to lie perpendicular to the pressing direction (Figure 2d). Contrarily, for the bulk polycrystalline sample of $Bi_{13}S_{18}I_2$ that was synthesized via sintering randomly oriented Bi_2S_3 and BiI_3 powder, almost no anisotropy was observed (Supporting Information, Figure S2).

Having successfully synthesized and characterized both bulk and nano $Bi_{13}S_{18}I_2$ samples on a large scale, we studied their thermoelectric properties (Figure 3). First, the electrical conductivities (σ) of the so-called bulk $Bi_{13}S_{18}I_2$, nano $Bi_{13}S_{18}I_2$, and nano $Bi_{13}S_{18}I_2+2\%$ $BiCl_3$ samples all increased with ascending temperature, 313–788 K (Figure 3a). This was indicative of a semiconductor-like transport behavior. Nearly no anisotropy was found in σ of the bulk $Bi_{13}S_{18}I_2$ sample due to the random grain orientation (Supporting Information, Figure S5e–h). Contrarily, σ showed pronounced differences in two directions of the nanosamples (Figure 3a). σ of the undoped nanosample was similar with that of the bulk sample, while doping had induced a significant enhancement of σ in the nano $Bi_{13}S_{18}I_2+2\%$ $BiCl_3$ sample (Figure 3a). The carrier concentration (n_H) of undoped nanosample showed a steady increase as temperature rose (Figure 3b). This again corroborated the semiconductor-like characteristics. Upon doping of $BiCl_3$, n_H was higher than that of the undoped nanosample over the whole temperature range (Figure 3b; Supporting Information, Table S2).

The Seebeck coefficients (S, Figure 3c) of all the samples had negative signs throughout the temperatures of interest, indicating that electron was the majority carrier. The nano and bulk undoped samples exhibited quite similar Seebeck coefficients (Figure 3c), implying their nearly identical carrier concentration. On the other hand, the lower magnitude of Seebeck coefficient of the $BiCl_3$-doped nanosample (Figure 3c; Supporting Information, Figure S10) compared to the undoped nanosample might be attributed to its higher carrier concentration (Figure 3b. The power factor was then calculated as $S^2\sigma$ (Figure 3d). The $BiCl_3$-doped sample exhibited a much larger (ca. 2 times) power factor compared with the undoped sample. The highest power factor attained in the nano $Bi_{13}S_{18}I_2+2\%$ $BiCl_3$ sample was 0.59 $mW\,m^{-1}\,K^{-2}$ at 788 K.

The total thermal conductivity (Figure 3e), κ_{total}, was calculated from $D_T \times C_p \times \rho$, in which D_T (thermal diffusivity; Supporting Information, Figure S9d) was measured using a laser flash method, C_p (specific heat; Supporting Information, Figure S9c) was assessed by differential scanning calorimetry (DSC) and ρ (mass density) was determined geometrically. For the bulk-grain sample, κ_{total} was 0.55 $Wm^{-1}K^{-1}$ at 363 K, and then decayed to 0.43 $Wm^{-1}K^{-1}$ at 763 K. For the nano $Bi_{13}S_{18}I_2+2\%$ $BiCl_3$ sample, the in-plane κ_{total} was 0.53 $Wm^{-1}K^{-1}$ at 313 K, and then decreased to 0.48 $Wm^{-1}K^{-1}$ at 788 K. The cross-plane κ_{total} of the nano $Bi_{13}S_{18}I_2+2\%$ $BiCl_3$ sample was even lower.

Combing all the transport properties, the maximum figure of merit, zT ($S^2\sigma T\kappa^{-1}$) of 1.0 was achieved at 788 K along the in-plane direction of nano $Bi_{13}S_{18}I_2+2\%$ $BiCl_3$ sample (Figure 3f). Along the cross-plane direction of this sample, zT_{max} was 0.8 at 738 K. The nano-undoped sample showed lower zT as compared to the doped sample in two directions. For the bulk undoped $Bi_{13}S_{18}I_2$, the highest zT attained was 0.7 at 763 K.

To elucidate the origin of the excellent figure of merit, we have conducted a series of theoretical studies. First, the electronic band structure (Figure 4a) is computed by density

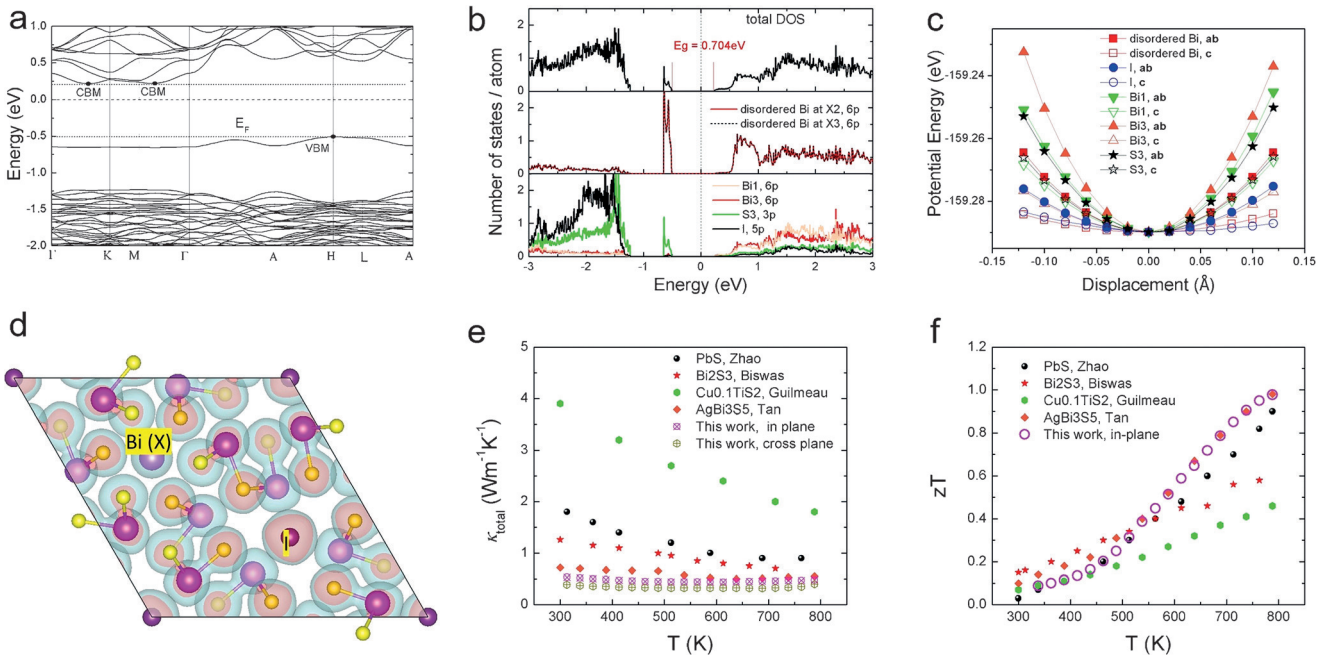

Figure 4. a) Electronic band structure, b) density of states, c) potential wells, and d) electron localization function. e),f) Comparison of e) κ_{total} and f) zT of our "nano $Bi_{13}S_{18}I_2+2\%$ $BiCl_3$" with those of PbS,[18] Bi_2S_3,[10a] $Cu_{0.1}TiS_2$,[10c] and $AgBi_3S_5$.[22]

functional theory (DFT; see the Supporting Information, Figure S1 for details). As seen from the total density of states (DOS, Figure 4b), the band gap (E_g) of $Bi_{13}S_{18}I_2$ is found to be around 0.70 eV, which is in good agreement with previous optical measurement (0.82 eV).[14] Intuitively, the alloying of Bi_2S_3 ($E_g = 1.3$ eV) and BiI_3 ($E_g = 1.67$ eV) would yield a compound with $E_g \approx 1.5$ eV. However, based on the analysis of orbital characters, the Bi(X) atoms with Bi–Bi bond contributed an in-gap state that is located at 0.70 eV below the conduction band minimum (CBM, Figure 4b), resulting in the anomalous shrinkage of the band gap. This E_g (0.70 eV) is within the proper range ($6–10\,k_B T$, 0.41–0.69 eV at 800 K) of those of typical mid-temperature thermoelectric materials, such as 0.31 eV of PbTe, 0.41 eV of PbS, and 0.86 eV of SnSe. The narrower band gap (0.70 eV) of $Bi_{13}S_{18}I_2$ as compared to that of Bi_2S_3 (1.3 eV) leads to the more favored activation of charge carrier and concomitant larger electrical conductivity (Supporting Information, Figure S5).

Deeper investigation unveils the double band extrema at the CBM (Figure 4a) that are located between the high symmetry points, Γ–M, and Γ–K, in the Brillouin zone (Supporting Information, Figure S1). They result in a very high valley degeneracy (N_v) of 12 in total (PbS, $N_v = 4$,[18] Bi_2S_3, $N_v = 2$[19]) and a moderate effective mass of electron, $m^* = 0.30\,m_0$ (PbS $0.39\,m_0$,[18] Bi_2S_3 $0.40\,m_0$[19]). This is attributable to the increased symmetry in $Bi_{13}S_{18}I_2$ (trigonal) as compared to Bi_2S_3 (orthorhombic). This high N_v can also be hinted from the extremely high Seebeck coefficient ($S = -400\ \mu V K^{-1}$ at 313 K (Figure 3c) with $n_H = 4.0 \times 10^{18}\ cm^{-3}$ (Figure 3b)) of our nano $Bi_{13}S_{18}I_2+2\%$ $BiCl_3$ sample as compared to those of other metal sulfide compounds ($-330\ \mu V K^{-1}$ of Bi_2S_3[20] and $-206\ \mu V K^{-1}$ of PbS[18]) with the same carrier concentration and similar effective mass. This is because S at a certain n_H increases with respect to $N_v^{2/3}$ and m^*.[21] These features would also favor a high power factor, as $S^2\sigma$ is proportional to N_v and inversely proportional to m^* at a certain carrier concentration.[21] Although our nano $Bi_{13}S_{18}I_2+2\%$ $BiCl_3$ sample had not been optimized in terms of carrier concentration, its peak power factor ($0.59\ mW m^{-1} K^{-2}$ at 788 K) is comparable to those of the reported metal sulfide thermoelectric compounds ($0.70\ mW m^{-1} K^{-2}$ for $AgBi_3S_5$[22]) and exceeds that of the optimized Bi_2S_3 materials ($0.47\ mW m^{-1} K^{-2}$).[23] We expect that through appropriate doping to tune the carrier concentration, an even higher power factor in $Bi_{13}S_{18}I_2$ may be achieved.

Besides the electrical transport, we have also studied the atomic vibrational properties that may lead to the low thermal conductivity. First, we obtain the potential wells using DFT (Figure 4c). The disordered Bi(X) and I atoms have the flattest potential wells as compared to S and other Bi atoms, especially along the c direction. This indicates that the Bi(X) and I atoms have much weaker bonding with their neighboring atoms than the other atoms have. Additionally, we have calculated the electron localization function (ELF) as displayed in Figure 4d. It is clearly seen that only the ELFs of the Bi(X) and I atoms are spherical, indicating their off-centering instability.[24] To directly observe their vibrations, we have conducted ab initio molecular dynamics (AIMD) simulations, and found that the amplitudes of vibration of Bi(X) and I atoms are much larger than other atoms. These data indicate that the Bi(X) and I atoms with relatively weak bonds may lead to low-energy optical modes. These flat optical modes have low group velocities and scatter other phonons much like so-called rattler modes.[24,25] As a result, the complex-structured bulk and nano $Bi_{13}S_{18}I_2$ have exceedingly low κ_l and κ_{total} as compared to state-of-the-art n-type

metal sulfide thermoelectric materials, such as Bi_2S_3,[10a] PbS,[18] TiS_2,[10c] and $AgBi_3S_5$[22] (Figure 4e).

According to the aforementioned theoretical analyses, $Bi_{13}S_{18}I_2$ has featured distinct electronic and phonon structure motifs that may be responsible for its high power factor, low thermal conductivity, and excellent thermoelectric properties. Although the bulk $Bi_{13}S_{18}I_2$ had not been optimized in terms of doping or nanostructuring, its peak zT (0.69) is comparable to that of the optimized Bi_2S_3 materials (0.72).[23] For the nanostructured $Bi_{13}S_{18}I_2$, doping, nano-grain boundary scattering (Supporting Information, Figure S12e) and texturization further improve its performance. The zT of our n-type nano $Bi_{13}S_{18}I_2 + 2\%$ $BiCl_3$ sample even outperformed that of n-type PbS[18] and was nearly identical with that of n-type $AgBi_3S_5$,[22] at 500–800 K (Figure 4f), without the use of scarce or toxic element. This peak zT of 1.0 is the highest up to date among n-type, environmentally friendly, and inexpensive thermoelectric metal sulfides.

Last but not least, as a strong candidate for mid temperature (500–800 K) thermoelectrics, our n-type $Bi_{13}S_{18}I_2$ holds great advantages in terms of toxicity, cost and processability, when compared with state-of-the-art n-type counterparts. PbQ[3,18] (Q = Te, Se, S) has used large amounts of toxic Pb. In half Heusler compound (HfZrNiSn),[26] MgSnGe[27] and In_4Se_3,[28] the use of expensive Hf ($607 kg^{-1}), Ge ($1250 kg^{-1}), or In ($520 kg^{-1}) impedes their widespread applications, whereas our $Bi_{13}S_{18}I_2$ consists of very cheap elements (Bi $17 kg^{-1}, S $0.09 kg^{-1}, and I $27 kg^{-1}). SnSe seems to have circumvented all the problems with a $zT = 2.2$ achieved in n-type single crystals[4] and zT around 1.0 obtained in n-type polycrystalline samples.[29] However, the constituent elements (Sn (2.2 ppm), Se (0.05 ppm)) still have much lower abundance than those of $Bi_{13}S_{18}I_2$ (S (500 ppm), I (0.49 ppm), Bi (0.05 ppm)) in the earth's crust. MgSiSn meets the criteria of both low cost and non-toxicity, yet requires high-temperature solid-state processing,[30] whereas our low-temperature, solution-phase procedure is energy-saving and time-efficient (only 4 h).

We finally demonstrate the chemical tunability by synthesizing analogous $Bi_{19}S_{27}Br_3$ nanorods and its nanostructured material (Supporting Information, Figure S11). We foresee that based on proper solution-phase methods, other open-framework compounds derived from canonical binary metal sulfides (selenides), such as $Sn_2BiS_2I_3$[31] and $Bi_{11}Se_{12}Cl_9$,[32] can be synthesized. This strategy can strongly modify the electronic band structure and the phonon transport, thus their thermoelectric properties can be improved. This will enrich the multinary metal sulfides (selenides) as a new family of eco-friendly, cost-efficient, and solution-processable thermoelectric materials.

Acknowledgements

Y.W. gratefully thanks the support from ACRI and a Herbert L. Stiles Professorship. X.R. thanks the support from DARPA (award number HR0011-15-2-0037). G.J.S. thanks the support from the Department of Energy (award number DE-SC0001299).

Conflict of interest

The authors declare no conflict of interest.

Keywords: band structures · bismuth · iodide · metal sulfides · thermoelectric

How to cite: *Angew. Chem. Int. Ed.* **2018**, *57*, 2413–2418
Angew. Chem. **2018**, *130*, 2437–2442

[1] G. Tan, L.-D. Zhao, M. G. Kanatzidis, *Chem. Rev.* **2016**, *116*, 12123–12149.
[2] S. I. Kim, K. H. Lee, H. A. Mun, H. S. Kim, S. W. Hwang, J. W. Roh, D. J. Yang, W. H. Shin, X. S. Li, Y. H. Lee, G. J. Snyder, S. W. Kim, *Science* **2015**, *348*, 109–114.
[3] Y. Pei, X. Shi, A. LaLonde, H. Wang, L. Chen, G. J. Snyder, *Nature* **2011**, *473*, 66–69.
[4] A. T. Duong, V. Q. Nguyen, G. Duvjir, V. T. Duong, S. Kwon, J. Y. Song, J. K. Lee, J. E. Lee, S. Park, T. Min, J. Lee, J. Kim, S. Cho, *Nat. Commun.* **2016**, *7*, 13713.
[5] X. Shi, J. Yang, J. R. Salvador, M. Chi, J. Y. Cho, H. Wang, S. Bai, J. Yang, W. Zhang, L. Chen, *J. Am. Chem. Soc.* **2011**, *133*, 7837–7846.
[6] Y. Zhang, J.-H. Bahk, J. Lee, C. S. Birkel, M. L. Snedaker, D. Liu, H. Zeng, M. Moskovits, A. Shakouri, G. D. Stucky, *Adv. Mater.* **2014**, *26*, 2755–2761.
[7] J. P. Heremans, V. Jovovic, E. S. Toberer, A. Saramat, K. Kurosaki, A. Charoenphakdee, S. Yamanaka, G. J. Snyder, *Science* **2008**, *321*, 554–557.
[8] L. Hu, T. Zhu, X. Liu, X. Zhao, *Adv. Funct. Mater.* **2014**, *24*, 5211–5218.
[9] B. Poudel, Q. Hao, Y. Ma, Y. Lan, A. Minnich, B. Yu, X. Yan, D. Wang, A. Muto, D. Vashaee, X. Chen, J. Liu, M. S. Dresselhaus, G. Chen, Z. Ren, *Science* **2008**, *320*, 634–638.
[10] a) K. Biswas, L.-D. Zhao, M. G. Kanatzidis, *Adv. Energy Mater.* **2012**, *2*, 634–638; b) Y. He, T. Day, T. Zhang, H. Liu, X. Shi, L. Chen, G. J. Snyder, *Adv. Mater.* **2014**, *26*, 3974–3978; c) E. Guilmeau, Y. Bréard, A. Maignan, *Appl. Phys. Lett.* **2011**, *99*, 052107.
[11] E. G. Tulsky, J. R. Long, *Chem. Mater.* **2001**, *13*, 1149–1166.
[12] D. B. Mitzi, L. L. Kosbar, C. E. Murray, M. Copel, A. Afzali, *Nature* **2004**, *428*, 299–303.
[13] J. Androulakis, S. C. Peter, H. Li, C. D. Malliakas, J. A. Peters, Z. Liu, B. W. Wessels, J.-H. Song, H. Jin, A. J. Freeman, M. G. Kanatzidis, *Adv. Mater.* **2011**, *23*, 4163–4167.
[14] R. Groom, A. Jacobs, M. Cepeda, R. Drummey, S. E. Latturner, *Chem. Mater.* **2017**, *29*, 3314–3323.
[15] D.-Y. Chung, T. Hogan, P. Brazis, M. Rocci-Lane, C. Kannewurf, M. Bastea, C. Uher, M. G. Kanatzidis, *Science* **2000**, *287*, 1024–1027.
[16] K. Yamana, K. Kihara, T. Matsumoto, *Acta Crystallogr. Sect. B* **1979**, *35*, 147–149.
[17] X. Shi, J. Yang, S. Bai, J. Yang, H. Wang, M. Chi, J. R. Salvador, W. Zhang, L. Chen, W. Wong-Ng, *Adv. Funct. Mater.* **2010**, *20*, 755–763.
[18] L.-D. Zhao, S.-H. Lo, J. He, H. Li, K. Biswas, J. Androulakis, C.-I. Wu, T. P. Hogan, D.-Y. Chung, V. P. Dravid, M. G. Kanatzidis, *J. Am. Chem. Soc.* **2011**, *133*, 20476–20487.
[19] P. Larson, V. A. Greanya, W. C. Tonjes, R. Liu, S. D. Mahanti, C. G. Olson, *Phys. Rev. B* **2002**, *65*, 085108.
[20] L.-D. Zhao, B.-P. Zhang, W.-S. Liu, H.-L. Zhang, J.-F. Li, *J. Solid State Chem.* **2008**, *181*, 3278–3282.
[21] Y. Pei, A. D. LaLonde, H. Wang, G. J. Snyder, *Energy Environ. Sci.* **2012**, *5*, 7963–7969.
[22] G. Tan, S. Hao, J. Zhao, C. Wolverton, M. G. Kanatzidis, *J. Am. Chem. Soc.* **2017**, *139*, 6467–6473.

[23] Z. Liu, Y. Pei, H. Geng, J. Zhou, X. Meng, W. Cai, W. Liu, J. Sui, *Nano Energy* **2015**, *13*, 554 – 562.
[24] M. K. Jana, K. Pal, U. V. Waghmare, K. Biswas, *Angew. Chem. Int. Ed.* **2016**, *55*, 7792 – 7796; *Angew. Chem.* **2016**, *128*, 7923 – 7927.
[25] a) M. Christensen, A. B. Abrahamsen, N. B. Christensen, F. Juranyi, N. H. Andersen, K. Lefmann, J. Andreasson, C. R. H. Bahl, B. B. Iversen, *Nat. Mater.* **2008**, *7*, 811 – 815; b) M. K. Jana, K. Pal, A. Warankar, P. Mandal, U. V. Waghmare, K. Biswas, *J. Am. Chem. Soc.* **2017**, *139*, 4350 – 4353.
[26] S. Chen, K. C. Lukas, W. Liu, C. P. Opeil, G. Chen, Z. Ren, *Adv. Energy Mater.* **2013**, *3*, 1210 – 1214.
[27] W. Liu, H. S. Kim, S. Chen, Q. Jie, B. Lv, M. Yao, Z. Ren, C. P. Opeil, S. Wilson, C.-W. Chu, Z. Ren, *Proc. Natl. Acad. Sci. USA* **2015**, *112*, 3269 – 3274.
[28] J.-S. Rhyee, K. H. Lee, S. M. Lee, E. Cho, S. I. Kim, E. Lee, Y. S. Kwon, J. H. Shim, G. Kotliar, *Nature* **2009**, *459*, 965 – 968.
[29] Q. Zhang, E. K. Chere, J. Sun, F. Cao, K. Dahal, S. Chen, G. Chen, Z. Ren, *Adv. Energy Mater.* **2015**, *5*, 1500360.
[30] W. Liu, X. Tan, K. Yin, H. Liu, X. Tang, J. Shi, Q. Zhang, C. Uher, *Phys. Rev. Lett.* **2012**, *108*, 166601.
[31] S. M. Islam, C. D. Malliakas, D. Sarma, D. C. Maloney, C. C. Stoumpos, O. Y. Kontsevoi, A. J. Freeman, M. G. Kanatzidis, *Chem. Mater.* **2016**, *28*, 7332 – 7343.
[32] E. K. U. Eggenweiler, V. Kramer, U. Petasch, H. Oppermann, *Z. Kristallogr. Cryst. Mater.* **1999**, *214*, 264.

Manuscript received: January 1, 2018
Accepted manuscript online: January 22, 2018
Version of record online: February 5, 2018

Angewandte Chemie
Eine Zeitschrift der Gesellschaft Deutscher Chemiker

Supporting Information

Manipulating Band Structure through Reconstruction of Binary Metal Sulfide for High-Performance Thermoelectrics in Solution-Synthesized Nanostructured $Bi_{13}S_{18}I_2$

*Biao Xu[+], Tianli Feng[+], Matthias T. Agne, Qing Tan, Zhe Li, Kazuki Imasato, Lin Zhou, Je-Hyeong Bahk, Xiulin Ruan, G. Jeffery Snyder, and Yue Wu**

anie_201713223_sm_miscellaneous_information.pdf

Experimental Section

Reagents. $Bi(NO_3)_3 \cdot 5H_2O$ (99.999%), thioacetamide (99%), polyvinylpyrrolidone (PVP, M_w = 40,000), KBr (99%), KI (99%), $N_2H_4 \cdot H_2O$ (80%), $BiCl_3$ (99.999%), BiI_3 (99.999%) and formamide (99%) were purchased from Sigma Aldrich. Bi_2S_3 (99.999%) was purchased from Alfa Aesar. Acetone and ethanol were purchased from VWR.

Solution-phase synthesis of $Bi_{13}S_{18}I_2$ nanorod. 36 mmol (17.4626 g) of $Bi(NO_3)_3 \cdot 5H_2O$, 54 mmol (4.0570 g) of thioacetamide, 200 mmol (33.3200 g) of KI and 12.00 g of PVP were dissolved into 600 mL of formamide in a 1000 mL flask. Then the whole solution was heated up to 150°C under N_2 flow and then incubated at this temperature for 4 h.

Powder processing and spark plasma sintering. The solution-synthesized dispersion of nanorods was centrifuged and washed with acetone for 2 times. Then it was re-dispersed in an ethanol solution of 8% $N_2H_4 \cdot H_2O$ and stirred for 24 hrs. After this, the dispersion was centrifuged and washed by ethanol for 2 times. Then the slurry was vacuum dried and ground into fine powder using an agate mortar. The powder was filled into a phi-10 mm graphite die and loaded into a Spark Plasma Sintering system (Fuji-lx211, Fuji Electronic Industrial). The SPS parameters were set as follows: axial pressure: 40 MPa, sintering time: 5 min and temperature: 500 or 600°C.

To synthesize bulk $Bi_{13}S_{18}I_2$ samples (0#), commercial Bi_2S_3 and BiI_3 powders with weight ratio of 83:17 (molar ratio of 5.60:1.00) were mixed together, ground for 30 min in a nitrogen-filled glove box and then SPSed at 600°C (axial pressure: 40 MPa, duration: 5 min). Another weight ratio of 84:16 (molar ratio of 6.00:1.00) was also tried.

The SPS condition for nanostructured samples are listed as below:

Sample 1# (nano undoped): 6 grams of the nano powder, 500°C, axial pressure: 40 MPa, duration: 5 min.

Sample 2# (nano doped with 2% $BiCl_3$): 6 grams of the nano powder mixed with 0.12 g of $BiCl_3$, 600°C, axial pressure: 40 MPa, duration: 5 min

Characterizations X-ray diffraction (XRD) was conducted on a Rigaku Ultima U4 diffractometer, with Cu Kα radiation (λ = 1.5418 Å), at 40 kV and 44 mA. The crystal structures were refined using the Rietveld method against XRD data with the Fullprof software packages based on the previously published $Bi_{13}S_{18}I_2$ structures. For Rietveld refinement against XRD data, a shifted Chebyschev function and a Pseudo-Voigt profile function were applied to model the background and peak shape respectively. Scanning Electron Microscopy (SEM) images were acquired on a FEI Quanta 250, equipped with Energy Dispersion Spectra (EDS). Transmission Electron Microscopy (TEM) was recorded on a FEI Tecnai F20 at 200 kV and a FEI Titan Themis Cs-corrected TEM at 300 kV. Thin-section samples of the as-sintered pellet for HRTEM were cut using a focused ion beam (FIB, Helios Dual Beam, FEI). Sound velocity was measured in an ultrasonic instrument.

Transport measurement. The Seebeck coefficients (S) were measured in a Linseis LSR-3. The electrical conductivity (σ) was also measured in a Linseis LSR-3 using a four-probe configuration and re-confirmed by a Van der-Pauw method. The thermal conductivity (κ) was expressed as $\kappa = D_T \cdot C_p \cdot \rho$. Thermal diffusivity ($D_T$) was measured using laser flash method in a Linseis XFA 600. Specific heat (C_p) was measured in a Linseis differential scanning calorimeter (DSC) using sapphire as the standard. Mass density (ρ) was calculated from the sample mass and dimensions. Hall coefficients (R_H), carrier concentration (n_H) and resistivity (ρ) (Van der Pauw, 4-point probe) were measured simultaneously with a home-built instrument (Northwestern University) using a 2 T magnet with pressure-assisted Molybdenum contacts. The deviation of Seebeck coefficient is around 2%, electrical conductivity σ (5%) and thermal conductivity κ (5%). The combined uncertainty of zT ($S^2\sigma T/\kappa$) is around 15%.

DFT methods

The DFT simulation is implemented by VASP[1] with local density approximation (LDA).[2] The cutoff planewave energy is 400 eV. The energy convergence threshold is $1*10^{-7}$ eV. The force convergence threshold during ionic relaxation is $2*10^{-6}$ eV/Å. The DFT-relaxed lattice parameters are a=15.78 Å, c=4.06 Å, which agree well with the experimental a=15.65 Å and c=4.02 Å. The k-mesh is Γ-centered 5*5*20.

The atomic environment and chemical bonding are depicted in the main text. The numbering scheme of atoms is illustrated in Figure S1b. The disorder Bi atoms (X) are surrounded by S atoms, and are farthest from the I atoms.

We have tried the X2X2, X3X3, and X2X3 configurations in our DFT calculation (Figure S1c). The formation energies are -4.824195, -4.826980 and -4.831091 eV/atom, respectively. Since the X2X3 structure has the lowest formation energy, we use it to calculate the electronic band structure and the potential well.

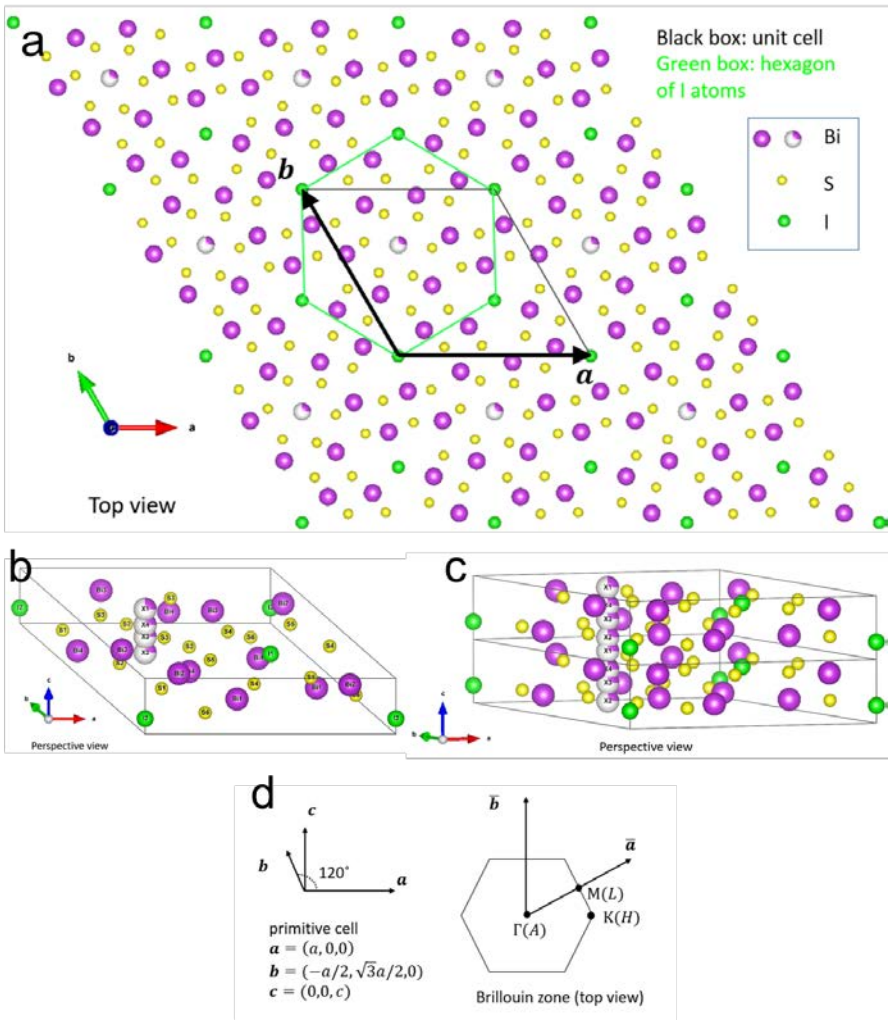

Figure S1. a) atomic structure viewed from [001] axis, b) a perspective view of the unit cell, c) a perspective view of a 1*1*2 super cell, d) illustration of the first Brillouin zone.

Characterizations on bulk-grain $Bi_{13}S_{18}I_2$

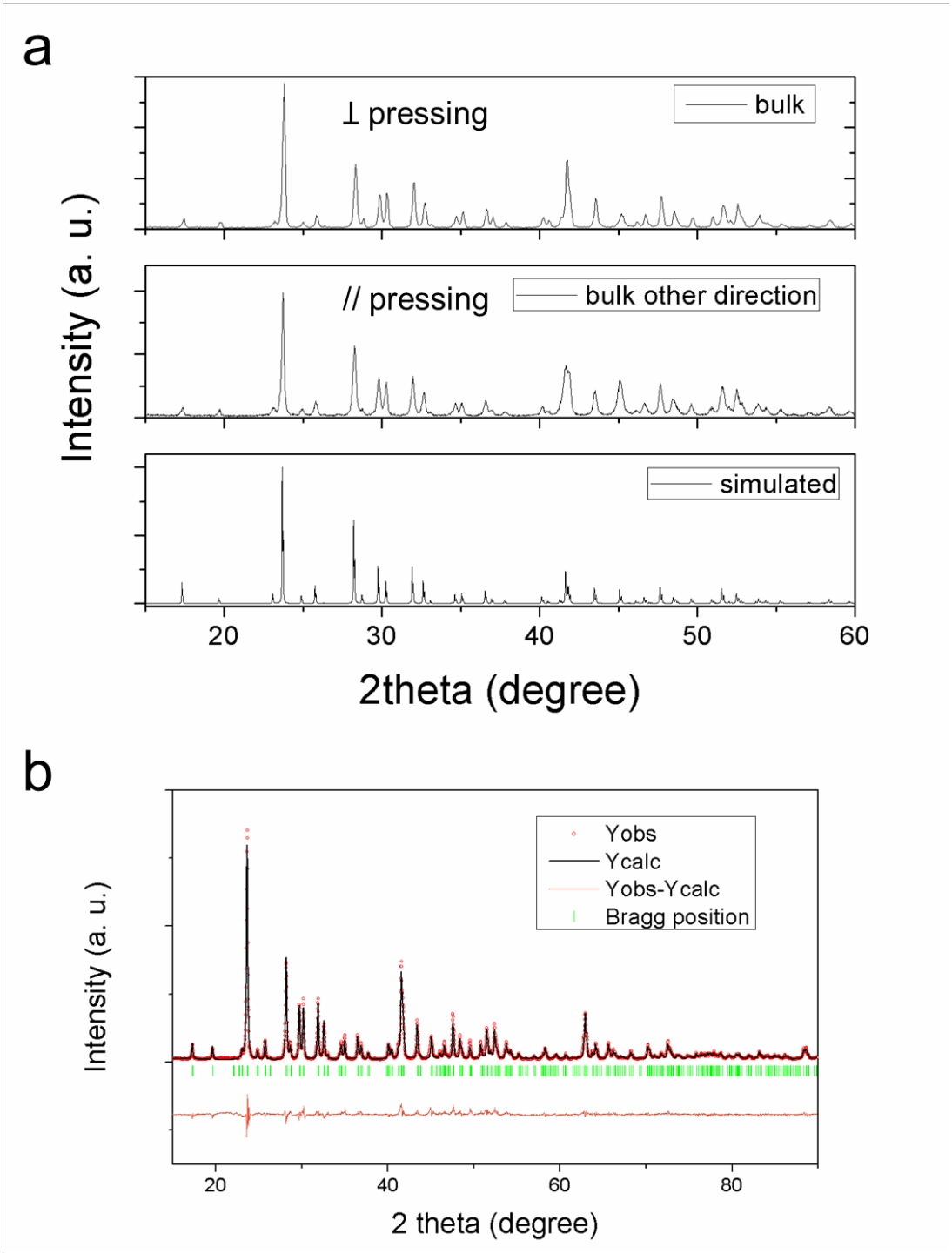

Figure S2 a) XRD pattern of bulk-grain $Bi_{13}S_{18}I_2$ in two directions (⊥ pressing vs // pressing), b) The refined XRD diffraction patterns by Fullprof program: calculated, observed, Bragg position and difference profiles are displayed by black line, red bubble, green vertical bar and orange line, respectively.

Table S1 The Rietveld refinement parameters for bulk-grain $Bi_{13}S_{18}I_2$

a (Å)	***b*** (Å)	***c*** (Å)	$\mathbf{R_p}$	$\mathbf{R_{wp}}$	$\mathbf{R_{exp}}$
15.650	15.650	4.021	6.63%	8.95%	3.98%

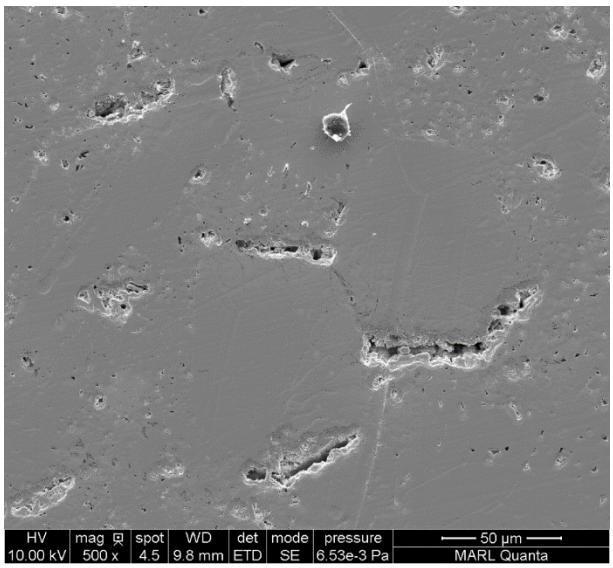

Figure S3. SEM second electron image of the bulk $Bi_{13}S_{18}I_2$ pellet.

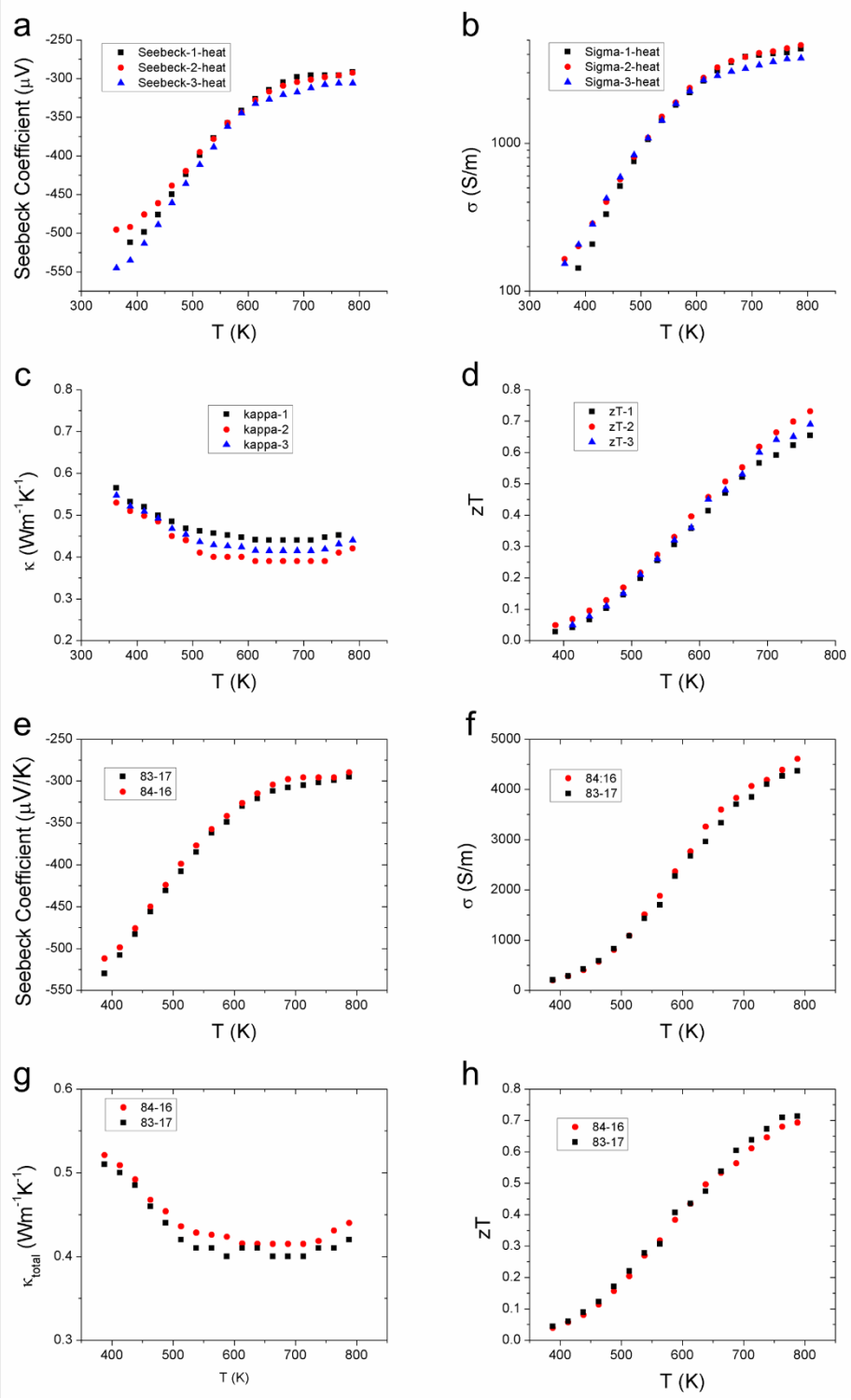

Figure S4. Thermoelectric property of three batches of bulk $Bi_{13}S_{18}I_2$ pellets: a) Seebeck coefficient, b) electrical conductivity, c) total thermal conductivity and d) zT. e) Seebeck coefficient, f) electrical conductivity, g) total thermal conductivity and h) zT of samples prepared from different weight ratios of Bi_2S_3: BiI_3 (84:16 (XRD: $Bi_{13}S_{18}I_2$ + 1% BiSI) and 83:17 (pure $Bi_{13}S_{18}I_2$), respectively).

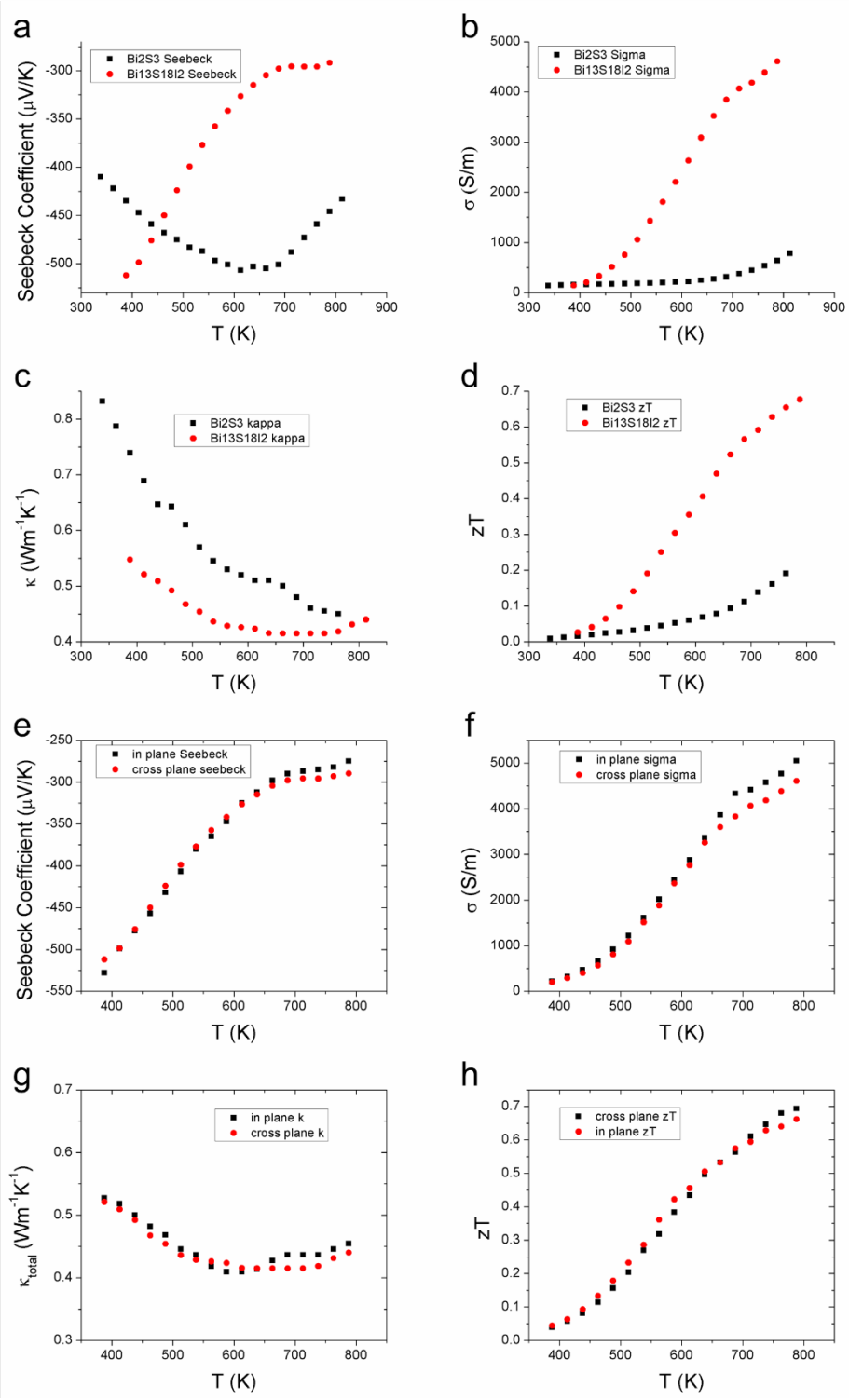

Figure S5. Comparison of thermoelectric properties between non-doped bulk $Bi_{13}S_{18}I_2$ and non-doped bulk Bi_2S_3: a) Seebeck coefficient, b) electrical conductivity, c) total thermal conductivity and d) zT. e) Seebeck coefficient, f) electrical conductivity, g) total thermal conductivity and h) zT, along the in-plane and cross-plane direction of bulk $Bi_{13}S_{18}I_2$.

Characterizations on $Bi_{13}S_{18}I_2$ nano powder and its as-SPSed nanostructured material

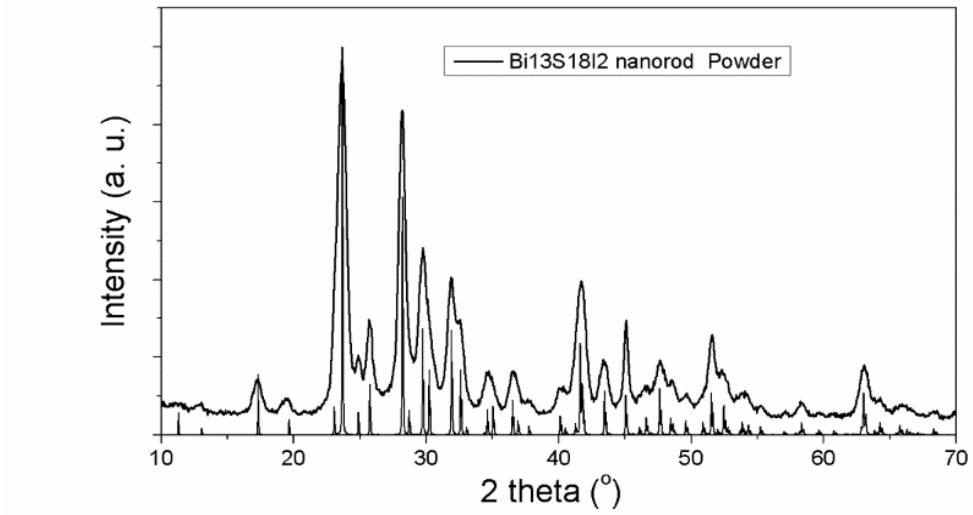

Figure S6. Powder X-ray diffraction pattern and simulated pattern of nano powder of $Bi_{13}S_{18}I_2$.

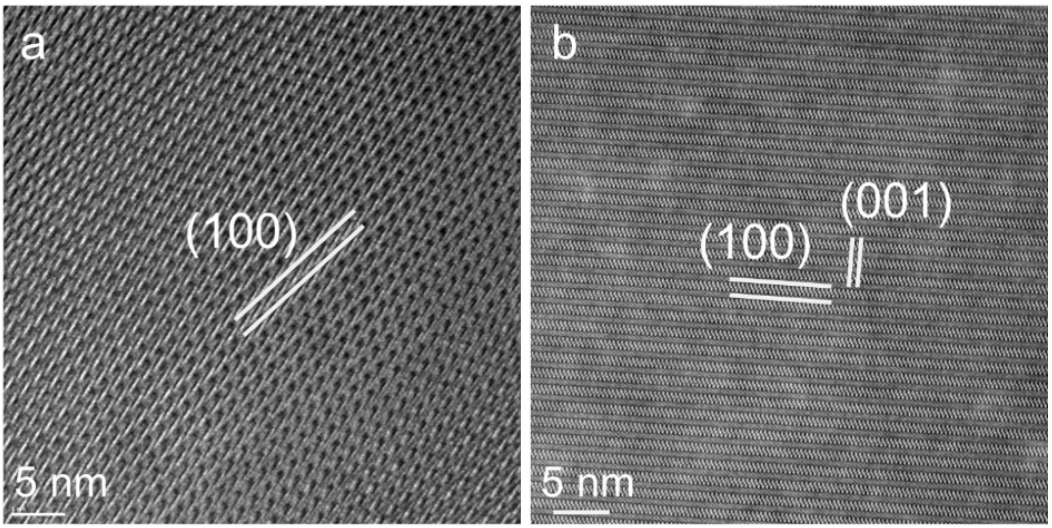

Figure S7. High resolution transmission electron microscopy image of the as-sintered nano $Bi_{13}S_{18}I_2$ pellet along a) [001] axis and HADDF STEM image along b) [010] axis.

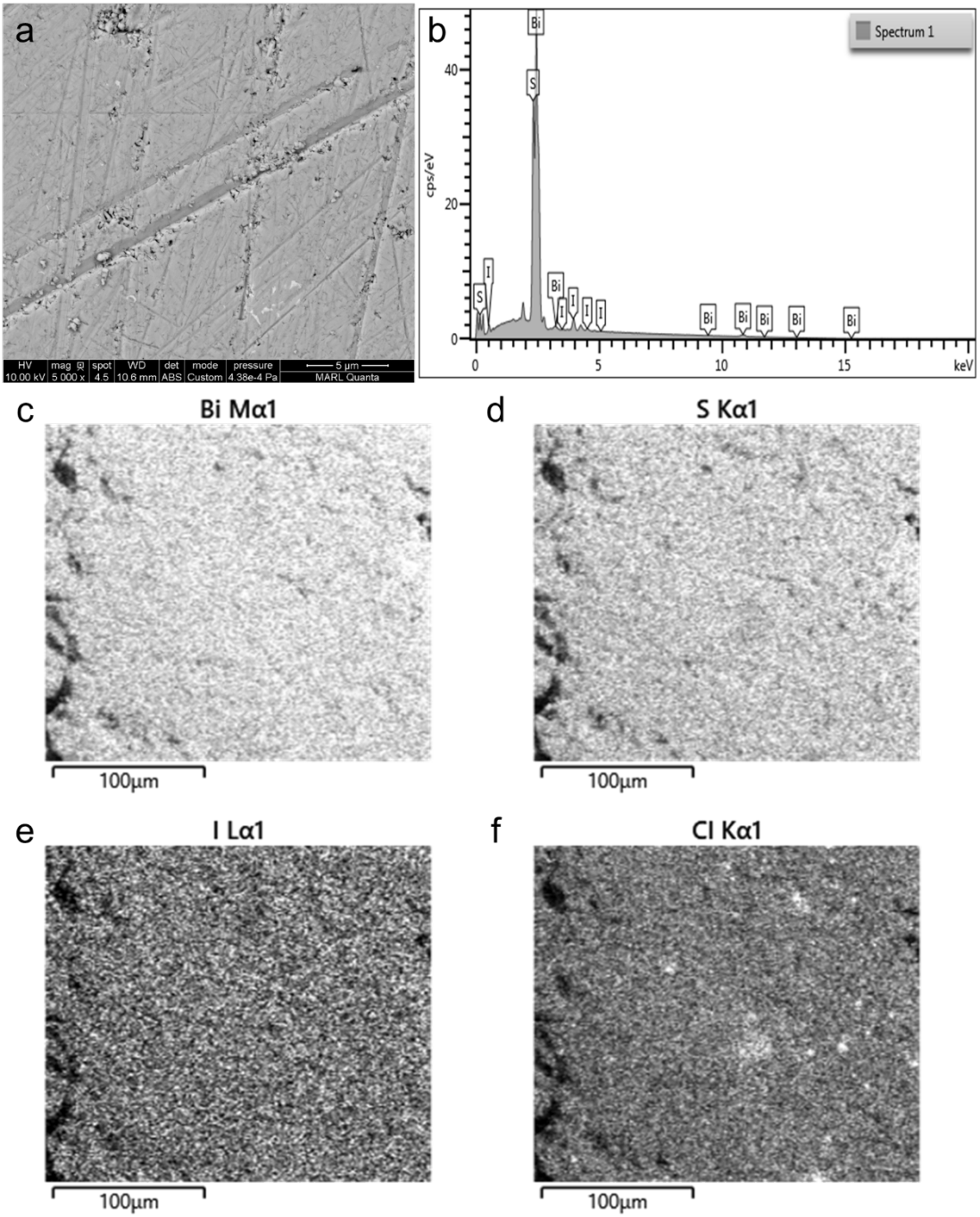

Figure S8. a) scanning electron microscopy image and b) energy dispersive spectrum of the as-pressed nano $Bi_{13}S_{18}I_2$ pellet. c)-f) EDS mapping of Bi, S, I and Cl of the mixture of nano $Bi_{13}S_{18}I_2$ powder and commercial $BiCl_3$ powder before sintering, the black areas were induced by shadowing.

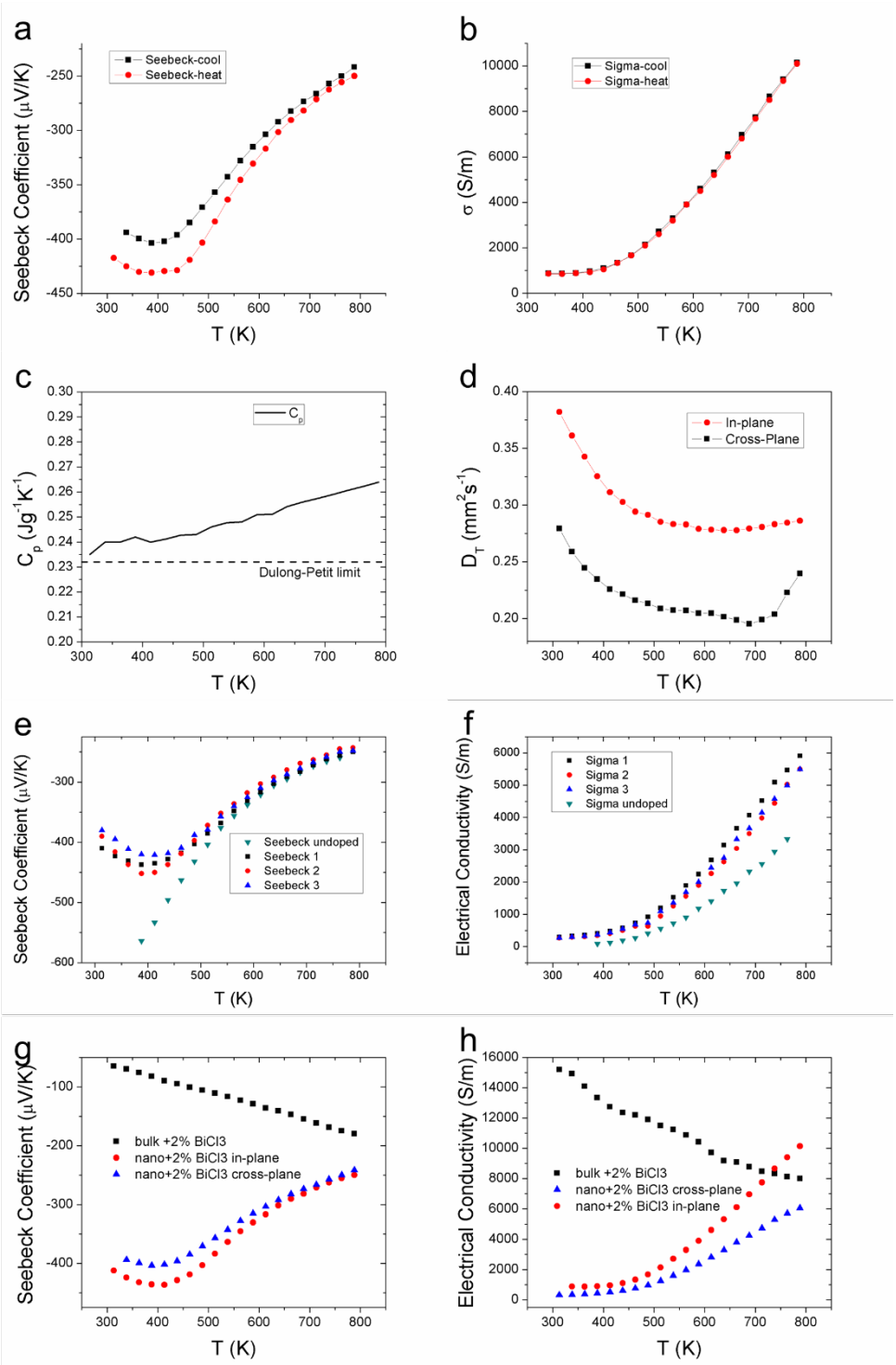

Figure S9. a) Seebeck coefficient and b) electrical conductivity of the 'nano $Bi_{13}S_{18}I_2$ + 2% $BiCl_3$' sample during heating and subsequent cooling, c) specific heat and d) thermal diffusivity of the 'nano $Bi_{13}S_{18}I_2$ + 2% $BiCl_3$' sample, e) cross-plane Seebeck coefficient and f) electrical conductivity of three bars cut along the pressing direction of a 'nano $Bi_{13}S_{18}I_2$ + 2% $BiCl_3$' and one bar from a 'nano $Bi_{13}S_{18}I_2$ undoped' cylinder, g) Seebeck coefficient and h) σ of bulk and nano $Bi_{13}S_{18}I_2$+ 2% $BiCl_3$ samples.

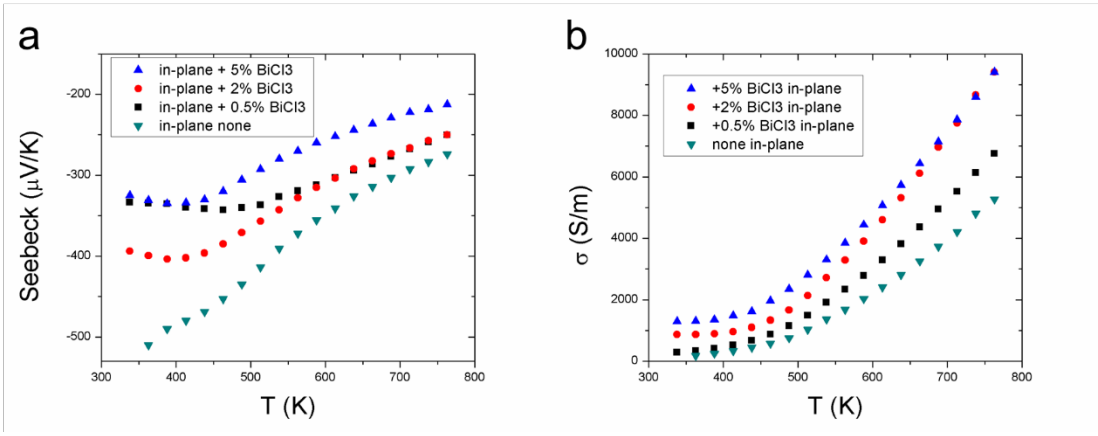

Figure S10. a) Seebeck coefficient and b) electrical conductivity of the nano $Bi_{13}S_{18}I_2$ sample with different amount of $BiCl_3$ added.

Table S2 Hall-effect carrier concentration (n_H, cm^{-3}) at various temperatures

	350 K	400 K	450 K	500 K	550 K	600 K
Nano $Bi_{13}S_{18}I_2$ none-doped	2.0×10^{18}	4.0×10^{18}	7.8×10^{18}	1.5×10^{19}	3.2×10^{19}	4.9×10^{19}
Nano $Bi_{13}S_{18}I_2$ + 2% $BiCl_3$	2.7×10^{18}	5.5×10^{18}	1.1×10^{19}	1.9×10^{19}	3.9×10^{19}	5.8×10^{19}

Characterizations of $Bi_{19}S_{27}Br_3$

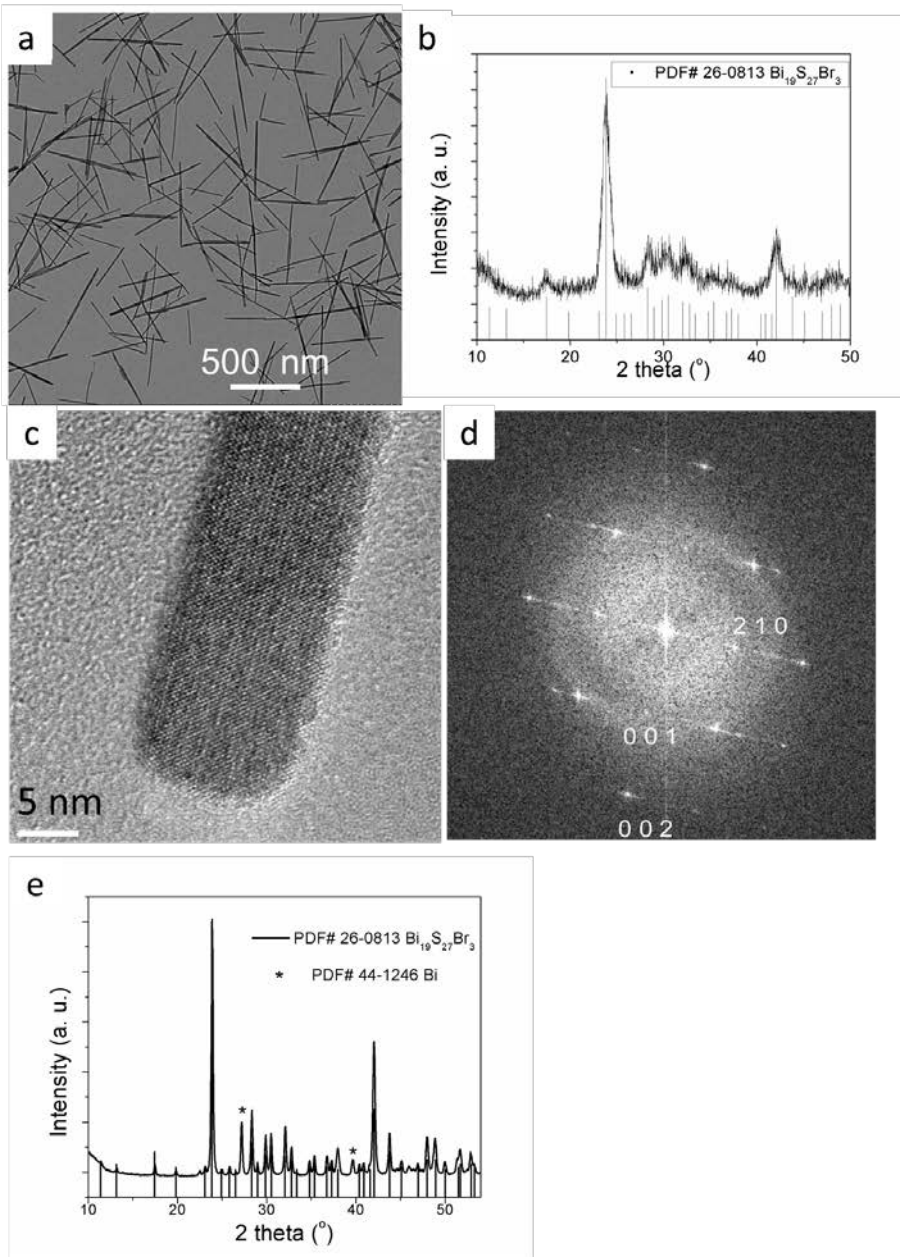

Figure S11 a) TEM, b) PXRD, c) HRTEM and d) fast Fourier transform images of the solution-synthesized $Bi_{19}S_{27}Br_3$ nanorod, e) PXRD pattern of as-sintered nanostructured $Bi_{19}S_{27}Br_3$ pellet.

Synthetic method of $Bi_{19}S_{27}Br_3$ nanorod

36 mmol (17.4626 g) of $Bi(NO_3)_3 \cdot 5H_2O$, 54 mmol (4.0570 g) of thioacetamide, 180 mmol (21.4204 g) of KBr and 12.00 g of PVP were dissolved into 600 mL of formamide in a 1000 mL flask. Then the whole solution was heated up to 150°C under N_2 flow and then incubated at this temperature for 4 h.

Thermal Conductivity Modelling

With the DFT lattice vibration analysis and the experimentally measured sound velocities, we can simulate the lattice thermal conductivity κ_l, according to the Debye-Callaway model:

$$\kappa_l = \frac{k_B}{2\pi^2 v_m}\left(\frac{k_B T}{\hbar}\right)^3 \int_0^{\theta_D/T} x^4 \frac{e^x}{(e^x-1)^2}\tau_{ph}\,dx \quad , \tag{1}$$

where x stands for $\frac{\hbar\omega}{k_B T}$, ω is the phonon frequency and τ_{ph} is the phonon relaxation time. In this model, the phonon branches are simplified to a single effective branch with the averaged group velocity v_m and maximum frequency $\omega_{max} = \frac{k_B \theta_D}{\hbar}$. θ_D is the Debye temperature calculated by:

$$\theta_D = \frac{h}{k_B}\left(\frac{3}{4\pi V_a}\right)^{\frac{1}{3}} v_m \quad , \tag{2}$$

where V_a is the average volume per atom. The averaged group velocity v_m is calculated by:

$$v_m = \left[\frac{1}{3}\left(\frac{1}{v_l^3}+\frac{2}{v_s^3}\right)\right]^{-\frac{1}{3}} \quad , \tag{3}$$

where v_l (3076 m/s) and v_s (1722 m/s) are the longitudinal and shear sound velocities measured from experiments, respectively.

To retrieve the phonon relaxation time τ_{ph}, we need to analyze possible phonon scattering process in **bulk and nano $Bi_{13}S_{18}I_2$. Bulk $Bi_{13}S_{18}I_2$** suffers from the anharmonic, point-defect and grain-boundary scattering, similar to typical thermoelectric materials. Since the grain size is in the magnitude of several micrometers (Figure S3), the grain-boundary scattering is negligible. Bulk $Bi_{13}S_{18}I_2$ has a similar crystal structure as Bi_2S_3 but contains the additional rattling Bi (X) and I atoms that induce possible resonant scattering. Collectively, the relaxation time τ_{ph} in Eq.(1) is expressed by the Matthiessen's rule,

$$\tau_{ph}^{-1} = \tau_{anh}^{-1} + \tau_{def}^{-1} + \tau_{\mathrm{Res}}^{-1} \quad . \tag{4}$$

The anharmonic phonon scattering contains the Umklapp and Normal processes, with the total scattering rate given by:[3]

$$\tau_{anh}^{-1} = \frac{A}{M_a v_m^2}\frac{\hbar\omega^2 T}{\theta_D}\exp\left(-\frac{\theta_D}{3T}\right) \quad , \tag{5}$$

which contains a fitting parameter A.

The point defect scattering, related to the density of state $\frac{\pi}{2} g\omega^2 DOS(\omega)$, is simplified as the power law in the Debye approximation, with a fitting parameter B:[4]

$$\tau_{def}^{-1} = B\frac{V_a}{4\pi v_m^3}\omega^4 \quad . \tag{6}$$

The resonant scattering relaxation time can be derived from:[5]

$$\tau_{Res}^{-1} = \sum_i C_i \frac{\omega^2}{(\omega^2 - \omega_i^2)^2}, \quad (7)$$

where C_i are fitting parameters and ω_i are the frequencies of each rattler that are estimated from the DFT potential well calculation. By fitting the potential well as an oscillator $\frac{1}{2}k\delta^2$ with k and δ representing the spring constant and displacement, respectively, the vibration frequency is estimated as $\omega_i \sim \sqrt{k/m}$.[6]

The modeling of the '**nano $Bi_{13}S_{18}I_2$** with 2% $BiCl_3$' sample is more complicated than that of bulk material due to the crystallographic anisotropy. For the bulk material, the averaged group velocity and Debye temperature are used for the modeling of the isotropic thermal conductivity, which originates from the random orientation of the crystal grains. However, in the nano samples, the orientation of crystal grains is not random, thus the thermal conductivity is anisotropic. The cross-plane direction of the sample is dominated by the [hk0] directions, and the in-plane direction of the sample features the preference of crystallographic c axis ([001] direction). Based on the experimental measurement, the sound velocities in different crystalline directions are nearly the same. Therefore, we can use the same averaged velocity v_m in all directions. Since the unit cell is anisotropic, the maximum acoustic frequency $\omega_{\max}$ value is anisotropic, which is reflected in the anisotropy of the Debye temperature $\theta_D = \frac{\hbar\omega_{\max}}{k_B}$. Thus, the ratio between the Debye temperatures in the ab plane and along c axis is expressed as:

$$\frac{\theta_{D,ab}}{\theta_{D,c}} = \frac{\omega_{\max,ab}}{\omega_{\max,c}}. \quad (8)$$

The single eq. (8) is not sufficient to determine the two variables $\theta_{D,ab}$ and $\theta_{D,c}$. Thus, we need more equations. The isotropic thermal conductivity of Bulk $Bi_{13}S_{18}I_2$ with random grain orientations should be the same as the averaged anisotropic thermal conductivity of the same Bulk $Bi_{13}S_{18}I_2$ but with ordered grain orientations:

$$\int_0^{\theta_D/T} x^4 \frac{e^x}{(e^x-1)^2}\tau_{ph}dx = \frac{2}{3}\int_0^{\theta_{D,ab}/T} x^4 \frac{e^x}{(e^x-1)^2}\tau_{ph}dx + \frac{1}{3}\int_0^{\theta_{D,c}/T} x^4 \frac{e^x}{(e^x-1)^2}\tau_{ph}dx. \quad (9)$$

Here the τ_{ph} include all the scattering mechanisms in the bulk samples. From Eq. (8) and Eq. (9), the two variables $\theta_{D,ab}$ and $\theta_{D,c}$ can be obtained. The results are $\theta_{D,ab} = 143$ K, $\theta_{D,c} = 286$ K.

With the anisotropic Debye temperatures determined, we can calculate the anisotropic thermal conductivity of nano $Bi_{13}S_{18}I_2$ with 2% $BiCl_3$ samples in two axes:

$$\kappa_{l,nano,cross-plane} = \frac{k_B}{2\pi v_m}\left(\frac{k_B T}{\mathrm{h}}\right)^3 \int_0^{\theta_{D,ab}/T} x^4 \frac{e^x}{(e^x-1)^2}\tau_{ph}dx \quad (10)$$

$$\kappa_{l,nano,in-plane} = \frac{k_B}{2\pi v_m}\left(\frac{k_B T}{\mathrm{h}}\right)^3 \int_0^{\theta_{D,c}/T} x^4 \frac{e^x}{(e^x-1)^2}\tau_{ph}dx \quad (11)$$

We can assume that the two directions have the same parameter B (defects). The difference originates from A, the anharmonic scattering and C, rattler modes.

Compared to the bulk counterpart, the nano $Bi_{13}S_{18}I_2$ has a smaller grain size around $D = 800$ nm. Thus, the phonon scattering should include an additional term, i.e., grain boundary scattering,

$$\tau_b^{-1} = \frac{v_m}{D}. \quad (12)$$

Collectively, $\tau_{ph}^{-1} = \tau_{anh}^{-1} + \tau_{def}^{-1} + \tau_{\mathrm{Res}}^{-1} + \tau_b^{-1}$. (13)

Table S4 Fitting Parameters in Modeling the Lattice Thermal Conductivity

	Bulk Bi_2S_3	Bulk $Bi_{13}S_{18}I_2$	Nano $Bi_{13}S_{18}I_2$ with 2% $BiCl_3$	
			Cross-plane	In-plane
A	19.2	20.6	10.6	36.6
B	0.10	0.035	0.06	
C_1	--	10 rad^2/ps^3	3 rad^2/ps^3	80 rad^2/ps^3
C_2	--	60 rad^2/ps^3	50 rad^2/ps^3	200 rad^2/ps^3

The electronic contribution to thermal conductivity, κ_e, is calculated as $L\sigma T$ according to the Wiedemann-Franz law, in which L is calculated from Boltzmann transport equation. The simulated κ_l is shown in Figure S12 in the supporting information, which agrees well with the experimental value (κ_{total} - κ_e).

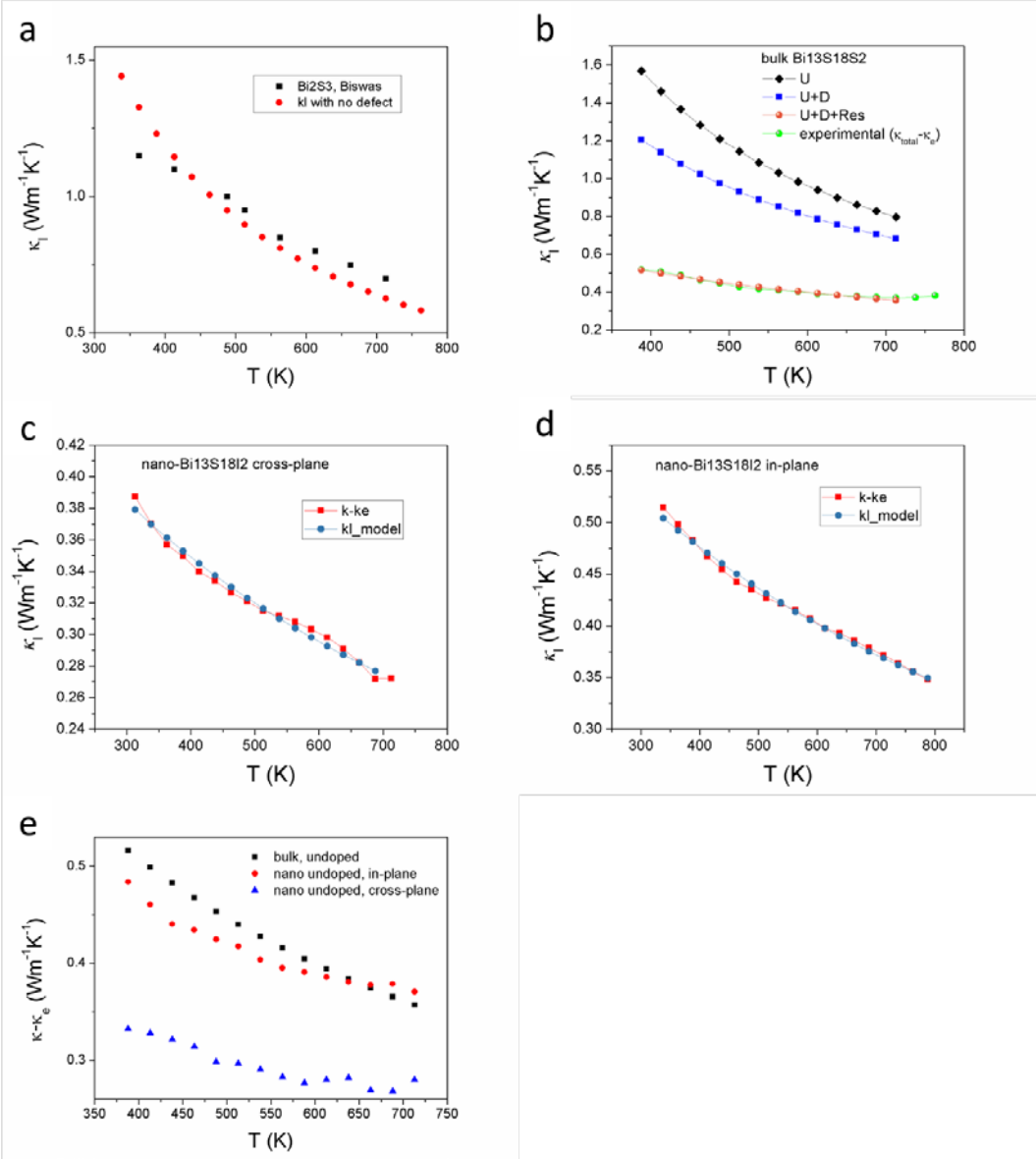

Figure S12. a) simulated κ_l (red dots) of bulk Bi_2S_3 as compared with the experimental value (black squares) in the literature,[7] b) lattice thermal conductivity modeling of bulk $Bi_{13}S_{18}I_2$ with Umklapp (U), defect (D) and resonant scattering (Res), lattice thermal conductivity modeling of 'nano $Bi_{13}S_{18}I_2$ + 2%$BiCl_3$' sample in the c) cross-pane and d) in-plane direction, e) lattice thermal conductivity of 'bulk $Bi_{13}S_{18}I_2$ undoped', 'nano $Bi_{13}S_{18}I_2$ undoped in-plane' and 'nano $Bi_{13}S_{18}I_2$ undoped cross-plane' samples.

References in the supporting information

(1) Kresse, G.; Furthmüller, J. *Compt. Mater. Sci.* **1996**, *6*, 15.
(2) Kohn, W.; Sham, L. J. *Phys. Rev.* **1965**, *140*, A1133.
(3) Slack, G. A.; Galginaitis, S. *Phys. Rev.* **1964**, *133*, A253.
(4) Klemens, P. G. *Proc. Phys. Soc. Sec. A* **1955**, *68*, 1113.
(5) Yang, J.; Morelli, D. T.; Meisner, G. P.; Chen, W.; Dyck, J. S.; Uher, C. *Phys. Rev. B* **2003**, *67*, 165207.
(6) Toberer, E. S.; Zevalkink, A.; Snyder, G. J. *J. of Mater. Chem.* **2011**, *21*, 15843.
(7) Biswas, K.; Zhao, L.-D.; Kanatzidis, M. G. *Adv. Energ. Mater.* **2012**, *2*, 634.